Check for updates

JGR Atmospheres

RESEARCH ARTICLE
10.1029/2024JD042294

Impact of Urbanization on Mesoscale Convective Systems: Insights From a Radar Wind Profiler Mesonet, Theoretical Analyses, and Model Simulations

Tian Xian[1], Jianping Guo[2], Runze Zhao[3], Xiaoran Guo[2], Ning Li[2], Yuping Sun[2], Zhen Zhang[2], Tianning Su[4], and Zhanqing Li[4]

[1]Faculty of Geographic Science, Beijing Normal University, Beijing, China, [2]State Key Laboratory of Severe Weather, Chinese Academy of Meteorological Sciences, Beijing, China, [3]National Satellite Meteorological Center (National Center for Space Weather), China Meteorological Administration, Beijing, China, [4]Department of Atmospheric & Oceanic Science and ESSIC, University of Maryland, College Park, MD, USA

Abstract The role of planetary boundary layer (PBL) in the urban effect on mesoscale convective systems (MCSs) remains highly uncertain. The high-density Mesonet of radar wind profilers (RWPs) in Beijing, along with geostationary satellite data from Fengyun-2, were used to investigate the MCS evolution and potential impact of urbanization. An MCS as observed by satellite tends to weaken over urban and downstream areas under strong precipitating conditions as opposed to an invigorated MCS over urban and downstream areas under weak precipitating conditions. The pattern of low-level convergence and high-level divergence from RWP Mesonet dominates the PBL of all MCS events under strong precipitating conditions, as compared with fluctuating vertical structures of convergence under weak precipitating conditions. Under strong precipitating conditions, turbulent friction weakens MCS activity over the Beijing urban area. Under weak precipitating conditions, thermal effect dominated over urban areas, favoring the formation of surface-level convergence and invigorating MCSs. Using the large-eddy simulation, we further investigated the influence of turbulent structural characteristics on the development of MCS. For the strong (weak) precipitating case, turbulence dissipation (buoyancy) dominated the turbulent kinetic energy over urban areas, explaining well the characteristics of MCSs propagating over these areas. Overall, the theoretical analysis and model simulation results confirm the observed impact of urbanization on MCSs. Besides the above scientific findings, our study highlights the importance of the RWP Mesonet in studying the urban effect on MCSs.

Plain Language Summary The influence of boundary-layer dynamics in urban underlying surface on mesoscale convective system (MCS) is still uncertain. Here, we explore the PBL dynamic characteristics of the evolution of MCSs in Beijing urban areas under different synoptic scale forcing by using the cloud products from geostationary satellites and the high-resolution RWP Mesonet measurements. In the case of strong precipitating conditions, low-level convergence and high-level divergence dominate the convective structure of PBL. In contrast, under weak precipitating condition, surface friction favors the formation of PBL convergence, which drives the development of MCS over urban and downstream areas. Further analysis based on WRF-LES model simulation verifies the observation phenomenon. The results obtained here will help us understand the dynamic impact of urbanization on cloud systems and provide new insights into the mechanism of urbanization affecting MCS.

Key Points:

- The dynamic structure of planetary boundary layer (PBL) is a key factor to determine the impact of urban on mesoscale convective system (MCS)
- Under strong (weak) precipitation conditions, low-level convergence and high-level divergence (fluctuating convergence) dominate the PBL
- Turbulence (surface) friction dominated over urban areas under strong (weak) precipitating conditions

Supporting Information:

Supporting Information may be found in the online version of this article.

Correspondence to:

J. Guo and Z. Li,
jpguocams@gmail.com;
zli@atmos.umd.edu

Citation:

Xian, T., Guo, J., Zhao, R., Guo, X., Li, N., Sun, Y., et al. (2024). Impact of urbanization on mesoscale convective systems: Insights from a radar wind profiler Mesonet, theoretical analyses, and model simulations. *Journal of Geophysical Research: Atmospheres*, *129*, e2024JD042294. https://doi.org/10.1029/2024JD042294

Received 22 AUG 2024
Accepted 29 NOV 2024

Author Contributions:

Data curation: Jianping Guo
Formal analysis: Tian Xian, Jianping Guo
Investigation: Tian Xian, Jianping Guo, Zhanqing Li
Methodology: Tian Xian, Jianping Guo, Runze Zhao, Xiaoran Guo, Tianning Su, Zhanqing Li
Resources: Jianping Guo, Runze Zhao
Software: Tian Xian, Runze Zhao, Ning Li, Yuping Sun, Zhen Zhang
Supervision: Jianping Guo, Zhanqing Li
Writing – original draft: Tian Xian
Writing – review & editing: Jianping Guo, Zhanqing Li

© 2024. The Author(s).
This is an open access article under the terms of the Creative Commons Attribution License, which permits use, distribution and reproduction in any medium, provided the original work is properly cited.

1. Introduction

Mesoscale convective system (MCS) is one of the main convective systems affecting the global hydrological cycle (Ai et al., 2016; Chen et al., 2019; Feng et al., 2016, 2021; Taylor et al., 2017). Globally, urbanization has been accelerating at an unprecedented pace, and its impact on Earth's weather and climate has been widely recognized (Chen & Frauenfeld, 2016; Kalnay & Cai, 2003; Qian et al., 2022; Sarangi et al., 2018; Zhang, Villarini, et al., 2018). It has been demonstrated that urbanization can significantly affect the exchanges of fluxes of momentum and heat between the surface and the lower troposphere (Hu et al., 2013; Shepherd et al., 2002; Zhang et al., 2017). This results in changes in surface air temperature and thermally induced circulations. Nevertheless, the ways and mechanisms by which the changes of urban or land use affect the evolution of MCS remain elusive (Theeuwes et al., 2019).

21698996, 2024, 24, Downloaded from https://agupubs.onlinelibrary.wiley.com/doi/10.1029/2024JD042294, Wiley Online Library on [01/03/2025]. See the Terms and Conditions (https://onlinelibrary.wiley.com/terms-and-conditions) on Wiley Online Library for rules of use; OA articles are governed by the applicable Creative Commons License

The measurements of vertical dynamic variables such as divergence and vertical velocity have been extensively used to indicate vertical motion and mesovortex in the MCS, which are generally calculated from rawinsonde or Doppler weather radar (Bousquet & Chong, 2000; Mapes & Houze, 1993, 1995). These measurements, especially in the planetary boundary layer (PBL), well characterize the structures and variation features of MCS (Bousquet & Chong, 2000). Nevertheless, the above-mentioned vertical observational studies associated with MCS were not conducted over urban areas.

The vertical profiles of thermodynamic and dynamic variables in the PBL over urban areas may help address this challenge facing the urban-MCS interaction. The PBL is the buffer for the exchange of heat and momentum between the surface, lower atmosphere, and clouds (Zhang, Guo, et al., 2018). Especially regarding urban-MCS interactions, process in the PBL is a key player driving the occurrence and enhancement of MCSs (Lorenz et al., 2019; Stull, 1988). Exceptional roughness of the urban landscape tends to increase boundary-layer convergence over and downwind of urban areas (Thielen et al., 2000; Yu et al., 2022). Shepherd et al. (2002) assessed the impact of the urban heat island (UHI) on convection, concluding that the UHI-induced secondary circulation contributed to the frequent occurrence of convective clouds in the downstream, particularly under calm conditions. However, if wind is strong enough, the turbulence generated by shear will suppress the heat transfer, inhibiting the influence of the UHI on convection (Huff & Changnon, 1973). While there have been many documented observations and numerical studies, the dynamics of urban-induced convection related to cloud dynamics are still poorly understood (Qian et al., 2022).

Turbulence is one of the main motion forms in the PBL, affecting the surface-atmosphere interaction by controlling the transport process in the atmosphere (Salesky et al., 2017). Studying turbulence structure in the PBL is helpful to understand its influence on various weather processes, especially clouds and precipitation (Han et al., 2019; Lee et al., 2019; Stull, 1988). Using large-eddy simulations (LESs), a lot of insights have been gained on the impact of urban surface on the turbulent structure and mixing processes in the PBL (Miao & Chen, 2008; Noh et al., 2003; Rai et al., 2017). Moreover, it is well recognized that the radar wind profiler (RWP) is able to continuously monitor turbulence profiles in the middle and lower troposphere (Solanki et al., 2022; Uma & Rao, 2009).

In this context, the main purpose of this study is to investigate the dynamic mechanism of the urban impact on MCSs by combining geostationary satellite and RWP observations, along with LES. In particular, we aim to distinguish the relative importance of different dynamic characteristics in different synoptic types. The paper is organized as follows. Section 2 describes the data, methods, and Weather Research and Forecasting (WRF) LES (WRF-LES) settings. Section 3 analyzes and discusses observations and simulation results. Conclusions and discussion are given in Section 4.

2. Data and Methods

2.1. Radar Wind Profiler, Millimeter Cloud Radar, and Surface Synoptic Observations

Beijing, the capital of China, is a megacity with a large population and a high degree of urbanization, located southeast of the Yanshan mountain range. The special topography, complex urban structure, and heterogeneous surface land-cover types make it particularly challenging to investigate land-atmosphere interactions. In this study, a variety of observational data sets during the warm-season months of May to September for the period 2018 to 2019 collected in Beijing (Figure 1) from the China Meteorological Administration (CMA), in combination with the European Centre for Medium-Range Weather Forecasts (ECMWF) Reanalysis v5 (ERA-5) (Hersbach et al., 2023), are used to analyze the physical process of MCSs above the heterogeneous surface.

Vertical profiles of wind and cloud radar reflectivity are provided by high-vertical-resolution RWPs and millimeter cloud radars (MMCR; Figure 1a), with time resolutions of 6 and 1 min, respectively (Guo et al., 2021; Y. Zhang et al., 2019a, Z. T. Zhang et al., 2019b). Wind speed and direction information is provided by the wind profiler, temperature, and RH is provided by the sounding measurement at the Beijing observatory station (39.80°N and 116.47°E, marked in Figure 1a). Hourly meteorological measurements are obtained from CMA's meteorological stations, including 10 m wind speed, precipitation, cloud fraction, and sea-level pressure (see the purple dots in Figure 1b). Hourly 2 m temperature (T_{2m}) is provided by the automatic weather stations (AWS, Figure 1b).

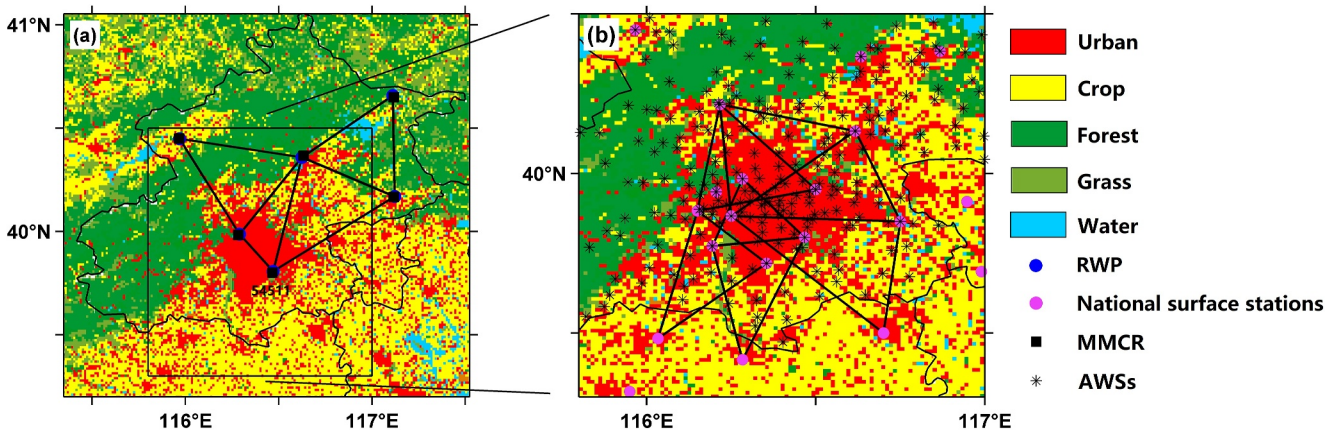

Figure 1. Satellite-based classification of panel (a) land-cover and land-use types in and around Beijing in 2020. Also marked are the locations of radar wind profiler (RWP) stations (blue dots) and millimeter cloud radar (MMCR) stations (squares). (b) A close view of the central urban area, showing national surface stations (purple dots) and automatic weather stations (AWS; stars). Black solid triangles are used to calculate divergence (a) and geostrophic wind (b).

2.2. Identification and Tracking of MCS

MCS is defined based on the cloud top temperature (CTT) of the Fengyun-2 (FY-2) F-series geostationary satellite (NSMC, 2023), which refers to a convective system with CTT less than 235 K, with a maximum cloud area greater than 10,000 km^2 and less than 160,000 km^2 and a duration of ≥3 hr. The tracking algorithm of MCS follows the method of Chen et al. (2019), which combines the Kalman filtering (KF) method with the traditional area overlap (AOL) method to determine the lifecycle of MCS. When the area of potential MCS is larger than 2,000 km^2, their spatial areas on continuous images will have some common pixels, so the AOL method can be used for tracking, and when the overlap rate is greater than 0.12, the clouds are regarded as the same cloud cluster at different times. However, for MCS with small area or fast movement speed, the AOL method is not applicable. Therefore, for these MCS, the KF equation is first used to predict their motion. Subsequently, locate the MCS closest to the predicted position in the next time point and match it with the current MCS. As a result, a total of 284 MCSs occurring on 134 days events passing through Beijing were identified.

2.3. Classification of Synoptic Patterns

This study applies the T-mode obliquely rotated principal component analysis (T-PCA) method to distinguish the dominant synoptic patterns covering the north China region (30°N–50°N, 107°E–127°E). T-PCA is an objective classification method based on principal component analysis and rotating T-mode principal components for loads. Compared with other classification methods such as neural network method (Agel et al., 2018; Maloney & Kiehl, 2002; Yang et al., 2022), correlation method (Lund, 1962), empirical orthogonal method (Nicholas & Battisti, 2012; Rana et al., 2019; Zveryaev, 2006), and classical principal component analysis method (Mills et al., 1994; Serra et al., 1996; Wei, 2012), the T-PCA has been widely used in the atmospheric circulation research (Huth et al., 2008; Miao et al., 2017; Xian et al., 2023; Zong et al., 2021).

Here the horizontal wind field and geopotential heights at the 850-hPa level are used in the T-PCA method for classifying dominant synoptic patterns, which are directly acquired from ERA-5 at 1,400 Beijing Time (BJT) when the PBL is fully developed (Guo et al., 2016; Zhang, Guo, et al., 2018). The reasons for selecting the 850-hPa potential height are twofold: (a) The Beijing and the surrounding areas have an elevation less than 1,500 m above sea level. (b) Based on high-resolution sounding measurements, the extreme weather events are typically linked to abnormal temperatures and humidity below 850-hPa (Yan et al., 2019). Here 9 clusters are chosen in the T-PCA method, five of which account for less than 6% of the MCS days analyzed and thus be discarded for further analysis. Therefore, only four dominant synoptic patterns are left, which collectively account for 75.4% of the MCS days analyzed.

21698996, 2024, 24, Downloaded from https://agupubs.onlinelibrary.wiley.com/doi/10.1029/2024JD042294, Wiley Online Library on [01/03/2025]. See the Terms and Conditions (https://onlinelibrary.wiley.com/terms-and-conditions) on Wiley Online Library for rules of use; OA articles are governed by the applicable Creative Commons License

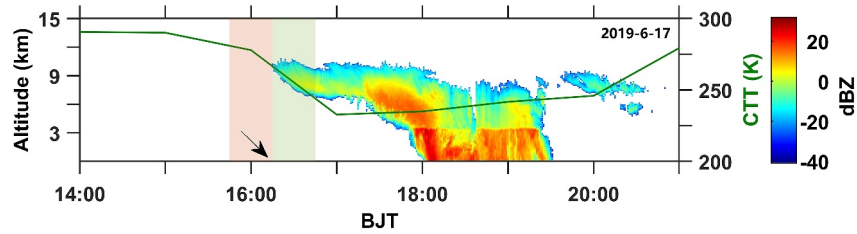

Figure 2. Time-altitude cross-section of radar reflectivity (color shading) observed by the cloud radar in Beijing on 17 June 2019. Also overlaid is the time series of the cloud-top temperature (CTT; green line) observed by the Fengyun-2 satellite. Horizontal divergence retrievals from radar wind profilers are taken during 30-min periods, being 30 min ahead of the appearance of clouds above Beijing. Note that the cloud-base height is estimated within the first 30 min of cloud radar observations (shaded in blue). Orange- and green-shaded vertical rectangles show the 30-min time periods before and after, respectively, the start time of the cloud object denoted by the black arrow.

2.4. Calculating the Profile of Area-Averaged Horizontal Divergence

Changes in roughness and surface temperature caused by the urban underlying surface represent changes in dynamic and thermodynamic characteristics, which usually changes the thermodynamics of the PBL in urban areas. To obtain vertical profiles of atmospheric dynamic variables, the areal averaged divergences at different levels ranging from the lower PBL up to middle troposphere are calculated from horizontal wind measurements from the RWPs. Bellamy. (1949) proposed the triangle method used in this study. Horizontal divergences in the triangular areas are calculated using horizontal wind observations from three noncollinear stations as follows:

$$D = \frac{(u_2 - u_1)(\Delta y_3 - \Delta y_1) - (u_3 - u_1)(\Delta y_2 - \Delta y_1) + (v_3 - v_1)(\Delta x_2 - \Delta x_1) - (v_2 - v_1)(\Delta x_3 - \Delta x_1)}{(\Delta x_2 - \Delta x_1)(\Delta y_3 - \Delta y_1) - (\Delta x_3 - \Delta x_1)(\Delta y_2 - \Delta y_1)} \quad (1)$$

where $(x_i, y_i)\ (i = 1,2,3)$ are the coordinates of the each vertex of the triangle. For this algorithm, it is also necessary to ensure that the side length of the triangle is greater than 40 km, the obtuse angles are less than 140°, and the area is greater than 500 km^2 (Guo, Guo, & Xian, 2023) to ensure the validity of the divergence retrievals. Therefore, according to the proposed algorithm, 6 RWPs and 4 triangles (Figure 1a) in the Beijing area were used for calculation.

2.5. Collocating MCSs Identified by FY-2 With RWP and MMCR Profiles

To obtain the dynamic structure of MCSs before convection initiation (CI), the start time of an MCS is found by matching FY-2 and MMCR observations. Figure 2 shows an example of a cloud object identified by the MMCR, with CTTs obtained from FY-2 observations. The RWP profile used to match wind profiles to the cloud object is shown as a black arrow at the start time of the cloud object. In addition, half an hour before (after) the start of the cloud object is used to calculate the divergence at the cloud base.

2.6. Isolating the Relative Contributions of Surface Friction and Turbulent Friction to MCSs

Compared with surrounding plain area, urban surface has relatively larger roughness, which tends to lead to stronger surface friction and enhanced convergence over the urban area. In contrast, turbulence friction can destroy the close coupling between the land surface and the atmosphere (Lee et al., 2019; Thielen et al., 2000). Therefore, separating turbulent friction and surface friction can help us understand the different processes behind the interactions between PBL and cloud with the urban underlying surface.

For stationary surface wind, the geostrophic balance is modified by friction as:

$$-\frac{\nabla P}{\rho} + F + f = 0 \quad (2)$$

where $-\frac{\nabla P}{\rho}$ represents the pressure gradient force (G), ρ is the air density (1.25 kg/m^3) and P is the sea-level pressure, which is obtained from surface meteorological station. F is the Coriolis force expressed as:

21698996, 2024, 24, Downloaded from https://agupubs.onlinelibrary.wiley.com/doi/10.1029/2024JD042294, Wiley Online Library on [01/03/2025]. See the Terms and Conditions (https://onlinelibrary.wiley.com/terms-and-conditions) on Wiley Online Library for rules of use; OA articles are governed by the applicable Creative Commons License

$$F = -2\Omega \times V \tag{3}$$

where V is obtained from wind measurements at 10 m weather tower and Ω is the rotational angular velocity of the Earth (7.292×10^{-5} rad/s).

In Equation 2, f is the drag force which is composed with both turbulent friction (f_t) and surface friction (f_s):

$$f = kV \tag{4}$$

where k is the drag coefficient.

In order to reflect the influence of surface roughness on observed surface wind speed under different synoptic patterns, we follow the method of Wu et al. (2016) here, assuming that the drag coefficient k is that of the 1980s and has not changed since then, and define the wind speed under this assumption as model wind speed (V_m):

$$-\frac{\nabla P}{\rho} + F + k_{1980s} V_m = 0 \tag{5}$$

Therefore, from Equation 5, it can be seen that due to the use of a fixed drag coefficient k_{1980s} (due to the inability to directly measure, k_{1980s} is calculated by bringing the observed wind speed into Equation 5), the variation of the model wind speed V_m is only controlled by the pressure gradient force G. The observed wind speed V is determined by the combined effects of pressure gradient force G, surface friction force f_s, and turbulent friction force f_t. So, the difference between V and V_m reflects the impacts of surface friction force and turbulent friction force on surface wind speed caused by changes in surface roughness around the research stations in recent years.

To obtain the contributions of f_s and f_t, we first need to calculate the V_m, and the calculation of $-\frac{\nabla P}{\rho}$ is crucial. Wu et al. (2016) provide a detailed calculation method of this. At a given surface meteorological station (purple dots in Figure 1b), sea-level pressure P is assumed to be a linear function of the station position (x, y) (Krueger et al., 2019; Zhang and Wang, 2020):

$$P = ax + by + c \tag{6}$$

Therefore, P at the three stations (see the triangles in Figure 1b) around a given station can be used to calculate ∇P and further calculate V_m. Here, we verified the correlation between the sea-level pressure calculated using the triangle method and the observed sea-level pressure, and found a high correlation between them ($R^2 = 0.998$, as shown in Figure S1 in Supporting Information S1), suggesting that this assumption is reasonable.

To attempt to quantify the influences of surface friction and turbulent friction, we followed the method proposed by Wu et al. (2018) and Y. Zhang et al. (2019a), Z. T. Zhang et al. (2019b) to separate these two forces. It is speculated that compared with cloudy days, sunny days are conducive to convection (Zhang, Guo, et al., 2018). Turbulence mixing is often significantly higher on sunny days than on cloudy days because both thermal turbulence and mechanical turbulence are stronger on sunny days, while cloudy days are primarily driven by horizontal wind vertical shear, which leads to mechanical turbulence. Therefore, following Wu et al. (2018) and Y. Zhang et al. (2019a), Z. T. Zhang et al. (2019b), weak mechanical turbulent mixing differences are assumed to be the same on clear- and cloudy-sky days. So, the comprehensive effect of pressure gradient force and turbulent friction force can be inferred from the difference in V between sunny and cloudy days. In addition, the difference in V_m on cloudy and clear days is a function of G only, so the influence of turbulent friction can be isolated by $\Delta V - \Delta V_m$, where Δ represents the difference in wind speed between the sunny and cloudy days. Because the combined effect of turbulent friction and surface friction can be expressed as $V - V_m$, the effect of the surface friction force can be finally calculated as $V - V_m - (\Delta V - \Delta V_m)$.

2.7. Turbulent Kinetic Energy (TKE) Budget

To analyze the turbulent structure characteristics under different synoptic forcing conditions, we further separate the vertical distribution of each term in the Turbulent Kinetic Energy (TKE) balance equation (Stull, 1988), which is shown as follows:

21698996, 2024, 24, Downloaded from https://agupubs.onlinelibrary.wiley.com/doi/10.1029/2024JD042294, Wiley Online Library on [01/03/2025]. See the Terms and Conditions (https://onlinelibrary.wiley.com/terms-and-conditions) on Wiley Online Library for rules of use; OA articles are governed by the applicable Creative Commons License

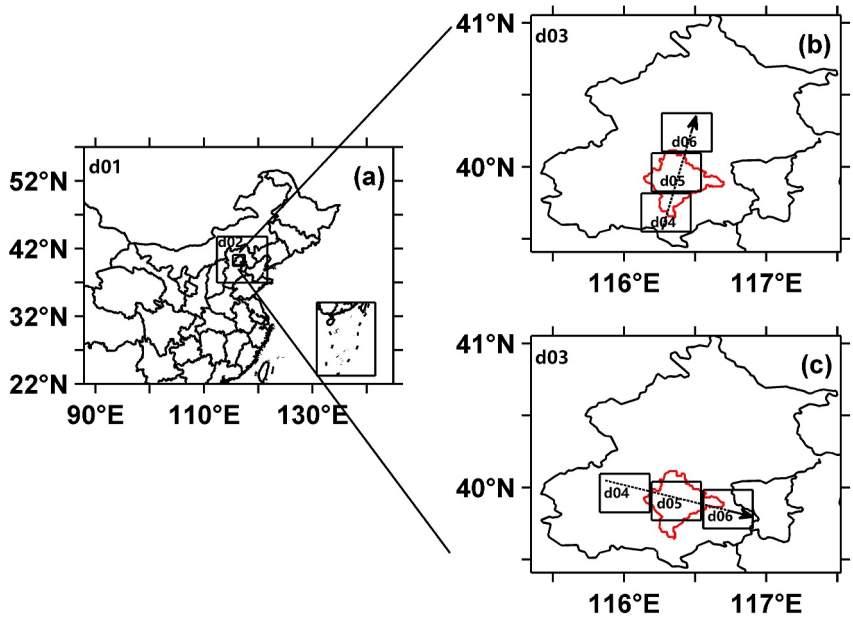

Figure 3. Maps of the (a) mesoscale simulation (d01 and d02) and (b)–(c) microscale simulation (d03–d06) domains. The inset maps on the right-hand side show the magnified d03–d06 domains, where numerical experiments are performed for (b) 11 July 2018 and (c) 1 September 2020, corresponding to weak and strong precipitating condition, respectively. Dotted arrows represent background prevailing wind directions.

$$\frac{\partial \overline{e}}{\partial t} = \underbrace{-\left[\overline{u'w'}\frac{\partial u}{\partial z} + \overline{v'w'}\frac{\partial v}{\partial z}\right]}_{\text{Shear}} + \underbrace{\frac{g}{\overline{\theta_v}}\overline{w'\theta_v'}}_{\text{Buoyancy}} \underbrace{-\frac{\partial \overline{w'e}}{\partial z} - \frac{1}{\overline{\rho_0}}\frac{\partial \overline{w'p'}}{\partial z}}_{\text{Diffusion}} \underbrace{-\varepsilon}_{\text{Dissipation}} \tag{7}$$

$$e = \frac{1}{2}\left(\overline{u'^2} + \overline{v'^2} + \overline{w'^2}\right) \tag{8}$$

where u', v', w' represent the velocity disturbance, ρ_0 is the standard density, θ_v is the virtual potential temperature, and e is TKE. On the right-hand side of Equation 7, there are four terms, representing the contribution of shear stress, buoyancy, diffusion, and turbulence dissipation, respectively. Each term of Equation 7 is separately calculated using the output from the WRF-LES model simulation, which is described in the next subsection.

2.8. WRF-LES Settings

The WRF model, version 4.1.5, is used to run LESs to explicitly solve the turbulence spatial structure of the convection process under different synoptic forcing conditions. Six WRF model domains are used: two mesoscale (Figure 3a, d01–d02) and four microscale (Figures 3b and 3c, d03–d06) domains, and LES is only performed at domain 03–06 (d03–06 in Figure 3). The grid dimensions for domain 01–06 are set as 481 × 481, 481 × 481, 591 × 591, 481 × 481, 481 × 481, and 481 × 481, corresponding to a grid spacing of 7.5 km, 1.5 km, 300 m, 60 m, 60 m, and 60 m, respectively, which are detailed in Table 1.

Compared with other parameterization schemes, the YSU scheme not only accounts for local diffusion but also well considers the nonlocal mixing caused by large-scale turbulent eddies and the entrainment process at the PBL top (Noh et al., 2003). Therefore, here the simulation domains d01–d02 use a first-order closure nonlocal Yonsei University (YSU) PBL parameterization scheme. When the grids spacing is much greater than the length scale of energetic turbulent vortices, turbulence is a subgrid process and requires the use of parameterization methods to simulate the turbulent transport process. When the grid spacing is much smaller than the length scale of the energy-carrying turbulent eddies, the model can directly resolve the energy-carrying turbulent eddies. In this case,

21698996, 2024, 24, Downloaded from https://agupubs.onlinelibrary.wiley.com/doi/10.1029/2024JD042294, Wiley Online Library on [01/03/2025]. See the Terms and Conditions (https://onlinelibrary.wiley.com/terms-and-conditions) on Wiley Online Library for rules of use; OA articles are governed by the applicable Creative Commons License

21698996, 2024, 24, Downloaded from https://agupubs.onlinelibrary.wiley.com/doi/10.1029/2024JD042294, Wiley Online Library on [01/03/2025]. See the Terms and Conditions (https://onlinelibrary.wiley.com/terms-and-conditions) on Wiley Online Library for rules of use; OA articles are governed by the applicable Creative Commons License

Table 1
Parameterization Schemes Used in WRF-LES

		Domain (one-way nest)			
Parameterization schemes	Step size	d01	d02	d03	d04–d06
Land-surface process		Noah land-surface	Noah land-surface	Noah land-surface	Noah land-surface
		Eta (1 September 2020)	Eta (1 September 2020)	Eta (1 September 2020)	Eta (1 September 2020)
Microphysics		NSSL 2-mom (11 July 2018)	NSSL 2-mom (11 July 2018)	NSSL 2-mom (11 July 2018)	NSSL 2-mom (11 July 2018)
Longwave radiation		RRTM	RRTM	RRTM	RRTM
Shortwave radiation		Dudhia	Dudhia	Dudhia	Dudhia
PBL		YSU	YSU	LES	LES
Cumulus		Kain-Fritsch	–	–	–
	Grid	481 × 481	481 × 481	591 × 591	481 × 481
	dx (m)	7,500	1,500	300	60
	dt (s)	25	5	1	0.2

Note. RRTM: rapid radiative transfer model; YSU: Yonsei University.

LES can be used for turbulence simulation. For the simulation domain d03–d06 with smaller grid spacing, the PBL scheme is turned off and LES is turned on. The TKE 1.5 closure scheme based on a prognostic equation for the subgrid-scale TKE, used to simulate the turbulence process. By adding more governing equations, the TKE 1.5 closure scheme have stronger physical constraints on turbulent transport. At this point, the dynamic process can directly resolve large-scale energetic, turbulent vortices, and only parameterize closure treatments for small-scale vortices (Smagorinsky, 1963). The other parameterization schemes used here are listed in Table 1.

In addition, it is generally optimal to use an aspect ratio equal to one in the WRF-LES model domain (Rai et al., 2017). This requires that the spacing between vertical grids is approximately equal to that between horizontal grids in the PBL. In this case, the whole model is set with 50 layers in the vertical direction, with a vertical grid spacing within the PBL of ~60 m. The d04–d06 domain is a subdomain of the d03 domain, which includes simultaneous turbulence simulations of the city in upwind and downwind directions.

Both WRF-Meso and WRF-LES model simulations were run for 30 hr. Weak and strong precipitating cases begin from 1,200 UTC on 31 August 2020 and 0600 UTC on 10 July 2018, respectively. Output from the WRF is saved every 10 min, with the initial and boundary conditions from the NCEP GDAS/FNL reanalysis data set on 0.25 × 0.25 degree grids.

2.9. Quantitating the Contribution of Thermodynamic Factors

The effect of thermal and dynamic factors on CTT was determined through multiple linear regression (Roy & Haigh, 2011) of the standardized variables, using the following equation:

$$CTT = \sum_{1}^{n} k_i x_i + c + \varepsilon \tag{9}$$

where x_i represents the thermodynamic factor, and the thermal factors include UHI, surface sensible heat flux, and T_{2m}, while the dynamic factors include vertical velocity disturbance ($\omega'\omega'$), horizontal velocity disturbance ($u'u'$), average divergence of 0–1 km, and average divergence of 1–3 km. k_i represents the correlation coefficient, c is the constant term and ε indicates the residuals of the equation. For each x_i, while controlling for other variables, the contribution of x_i can be separated by calculating the change in variance explanatory rate of the equation after removing the factor.

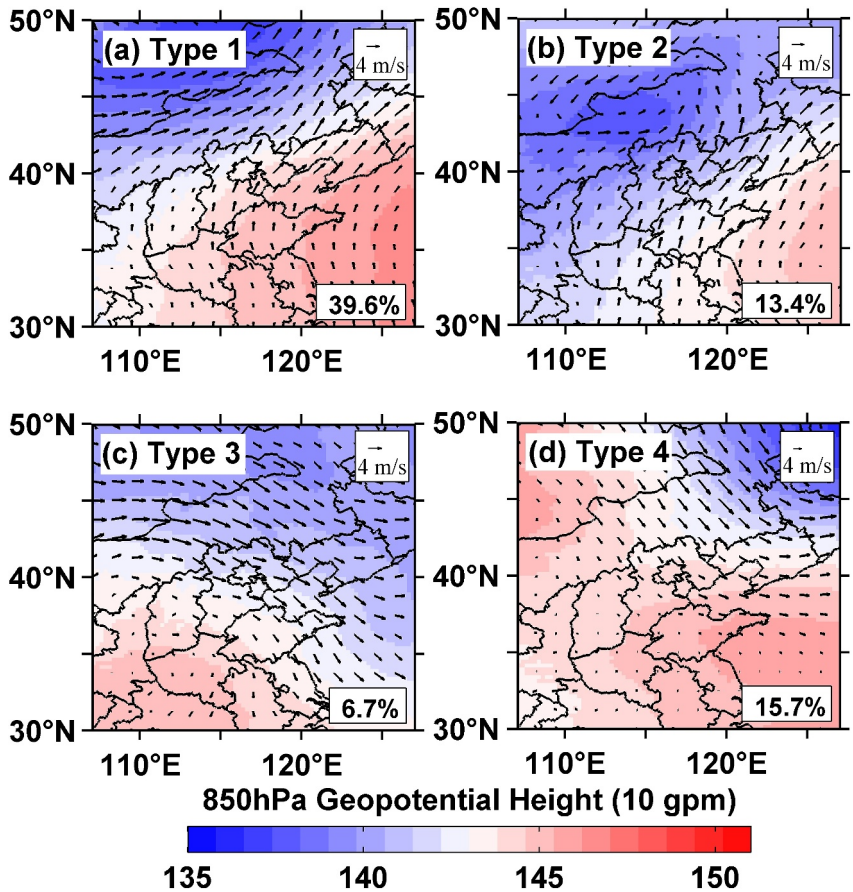

Figure 4. Four dominant synoptic patterns affecting mesoscale convective systems over Beijing were determined based on the geopotential height (color shading) and wind field (arrows) at 850-hPa using the T-PCA method. Each label in the lower right corner shows the percentage of each synoptic type.

3. Results and Discussion

3.1. MCS Features Observed by the FY-2 Geostationary Satellite in Relation to the Synoptic Forcing Pattern

The initiation, development, and dissipation of any MCS event are closely related to certain synoptic forcing patterns (Feng et al., 2021). To better isolate large-scale synoptic forcing from the potential impact of urbanization on MCSs, the synoptic forcing for each MCS event is first identified.

Figure 4 shows the four dominant synoptic patterns under which all MCS events occurred in Beijing during the warm season (from May to September) of 2018–2019. These four synoptic patterns can be roughly divided into two categories: strong precipitating and weak precipitating condition, both of which have two subtypes. Specifically, when the rainfall intensity of the first third and last third of the MCS rainfall event is higher (less) than the corresponding percentile rainfall intensity of all rainfall events (Figure S2 in Supporting Information S1), the corresponding large-scale weather pattern is considered a strong (weak) precipitating condition. Specifically, for all rainfall events, the lowest and highest one-third of the hourly rainfall intensity are 0.29 mm/hr and 1.52 mm/hr, respectively. Therefore, Type 1–2 correspond to strong precipitating pattern, whereas Type 3–4 correspond to weaker precipitating pattern.

Under the condition of synoptic pattern of Type 1 (Figure 4a), the region of interest is located near the periphery of the western Pacific subtropical high, a region with southwest winds. This favors the formation of MCS, which reaches up to 127 events passing over the Beijing metropolitan area. Under the condition of Type 2 (Figure 4b), Beijing straddles the boundary zone between a cyclonic system to the northwest and an anticyclonic system to the

21698996, 2024, 24, Downloaded from https://agupubs.onlinelibrary.wiley.com/doi/10.1029/2024JD042294, Wiley Online Library on [01/03/2025]. See the Terms and Conditions (https://onlinelibrary.wiley.com/terms-and-conditions) on Wiley Online Library for rules of use; OA articles are governed by the applicable Creative Commons License

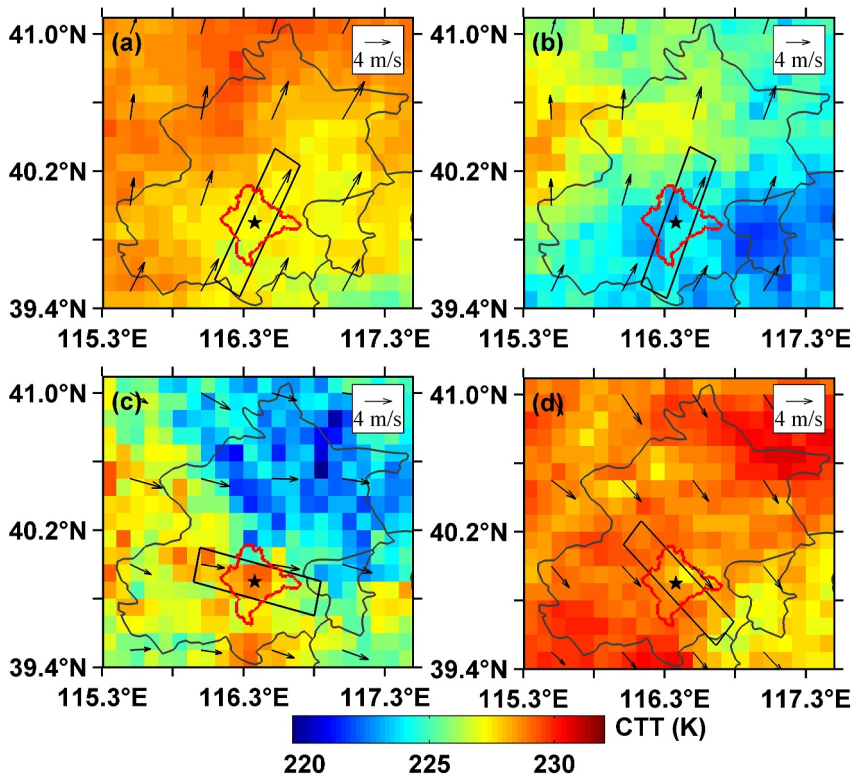

Figure 5. Spatial distribution of cloud top temperature (CTT) from the FY-2 geostationary satellite for the four synoptic patterns. Red polygon outlines the urban area of Beijing, and the black rectangle (100 km × 20 km) is used to describe the spatial gradient of CTT centered on the Beijing urban area under the prevailing wind for each synoptic pattern.

southwest. Similarly, MCS is more likely to occur under the influence of southwesterly winds, with a total of 49 MCS events passing over the Beijing metropolitan area under this synoptic pattern. Beijing is under the influence of a high-pressure system in the Type 3 weak precipitating case (Figure 4c). For the Type 4 weak precipitating case (Figure 4d), a uniform atmospheric pressure system dominates Beijing, which is unfavorable for the occurrence of severe weather. Therefore, there are fewer MCS events passing through Beijing metropolitan area under synoptic pattern Type 3 (15 events) and Type 4 (46 events).

It should be noted that the individual days within each synoptic pattern cluster may exhibit variability from the average pattern of the cluster. Averaging over all days can potentially smooth out synoptic disturbances or forcing that may be favorable for MCSs development.

Given the fact that the number of clusters chosen in the T-PCA method may impact the classification results, we conducted sensitivity analysis by changing the number of principal components from 9 to 5. The results for 5 dominant synoptic patterns are shown in Figures S3–S5 in Supporting Information S1, which do not significantly change the conclusions. Namely, under strong (weak) precipitating condition, urban tends to have an inhibition (enhancement) effect on the evolution of MCS.

3.2. MCS Evolution Associated With Urbanization

When dominated by strong (weak) precipitating condition, the average CTT along the urban prevailing wind shows a large upward (downward) trend (Figures 5 and 6), while the averaged area of MCS shows a significant downward (upward) trend (Figure S6 in Supporting Information S1). This suggests that the impact of the urban underlying surface on the vertical development of MCSs is sensitive to the prevailing wind direction and synoptic background. This also suggests that distinguishing the synoptic forcing is crucial to analyzing the impact of the heterogeneous underlying surface on clouds.

21698996, 2024, 24, Downloaded from https://agupubs.onlinelibrary.wiley.com/doi/10.1029/2024JD042294, Wiley Online Library on [01/03/2025]. See the Terms and Conditions (https://onlinelibrary.wiley.com/terms-and-conditions) on Wiley Online Library for rules of use; OA articles are governed by the applicable Creative Commons License

21698996, 2024, 24, Downloaded from https://agupubs.onlinelibrary.wiley.com/doi/10.1029/2024JD042294, Wiley Online Library on [01/03/2025]. See the Terms and Conditions (https://onlinelibrary.wiley.com/terms-and-conditions) on Wiley Online Library for rules of use; OA articles are governed by the applicable Creative Commons License

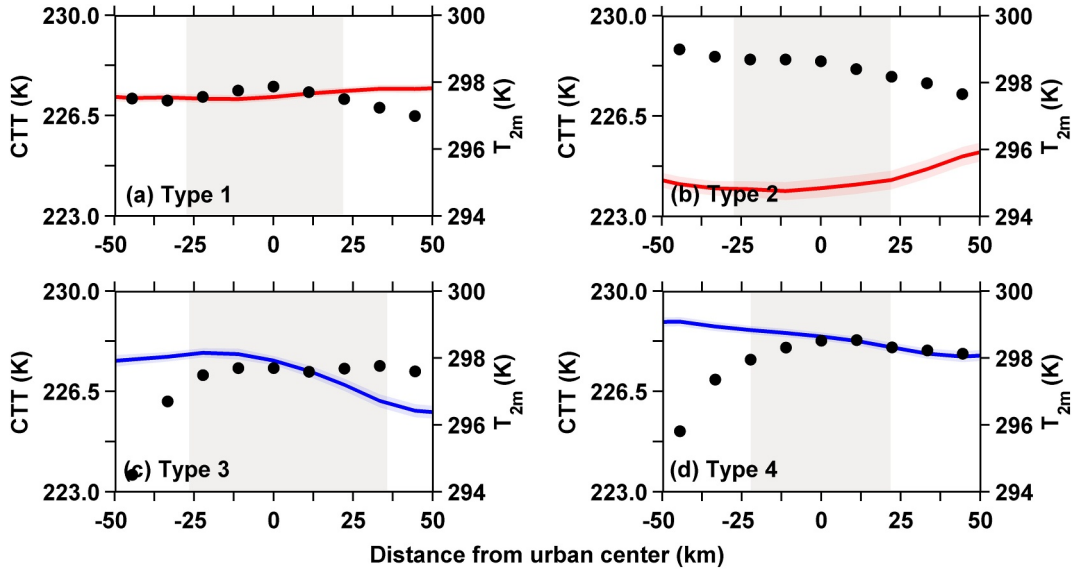

Figure 6. Spatial evolution of satellite-observed cloud-top temperature (CTT, solid line) and 2-m air temperature (T_{2m}, black dots) as calculated for all the mesoscale convective system samples that are located at one given location along the prevailing wind in the black rectangles shown in Figure 5 for the four different synoptic patterns: (a) Type 1, (b) Type 2, (c) Type 3, and (d) Type 4. The gray shading represents the urban area.

Why are the urbanization-induced decreases in CTT in the urban and downstream regions more remarkable when Beijing is under the influence of a weakly precipitating pattern? One reason may be that T_{2m} in urban areas are higher than upstream of these areas when weak precipitating condition dominates, that is, the UHI effect (Figure 7). To verify this, we divide the station UHI and sensible heat flux into two subgroups. As illustrated in Figure S7 in Supporting Information S1, driven by strong sensible heat fluxes (mean sensible heat flux = 55.3 W/m^2) under weak precipitating conditions, the thermal disturbance of the surface and the resulting urban circulation, or the downstream translation of convective clouds generated by the UHI, lead to cloud invigoration over urban and downstream areas (Kaufmann et al., 2007). At the same time, clouds are more likely to initiate in downstream areas of cities (Figures S8c and S8d in Supporting Information S1). The strong precipitating condition reduces the horizontal gradient of the temperature driving the circulation, potentially suppressing its influence on convection (Bornstein & Lin, 2000; Xian et al., 2023). In addition, under strong precipitating condition, MCS may also experience building-induced branching and detouring effects when passing through urban areas, which will weaken the strength of MCS and make it easier for it to disappear in upstream areas (Figures S8e and S8f in Supporting Information S1).

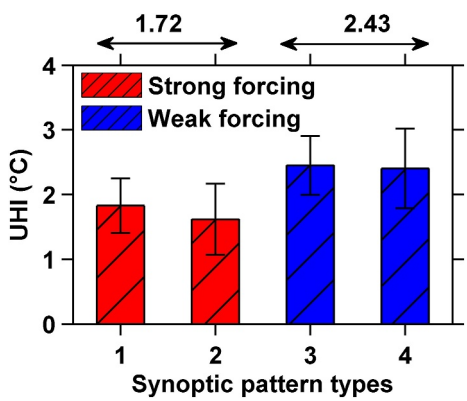

Figure 7. Histograms of urban heat island (unit: °C) in the Beijing area under strong (red) and weak (blue) precipitating conditions. Note that the numbers on the top of the bars represent the magnitudes of their corresponding UHIs.

3.3. Potential Contribution of Low-Level Dynamic Variables to MCSs

In fact, through interaction with thermodynamics, dynamics can also affect the development of MCS. On the one hand, larger roughness will be conducive to convergence over urban areas, promoting the development of convection. In addition, increasing turbulence with strong prevailing winds will weaken the dependence of clouds on the surface, thus reducing the impact of the UHI thermal disturbance in the boundary layer on clouds (Lee et al., 2019; Zhu et al., 2016). At the same time, the bifurcating effect of urban buildings will also lead to the splitting of convective clouds, ultimately weakening the development of clouds. Therefore, to evaluate the role of dynamic effects under strong and weak precipitating conditions, we use RWP measurements to calculate the vertical divergence profile under different synoptic forcing conditions.

Figure 8 shows vertical divergence characteristics before each MCS event. For each initiation, the start time is defined as the time of the signal detected

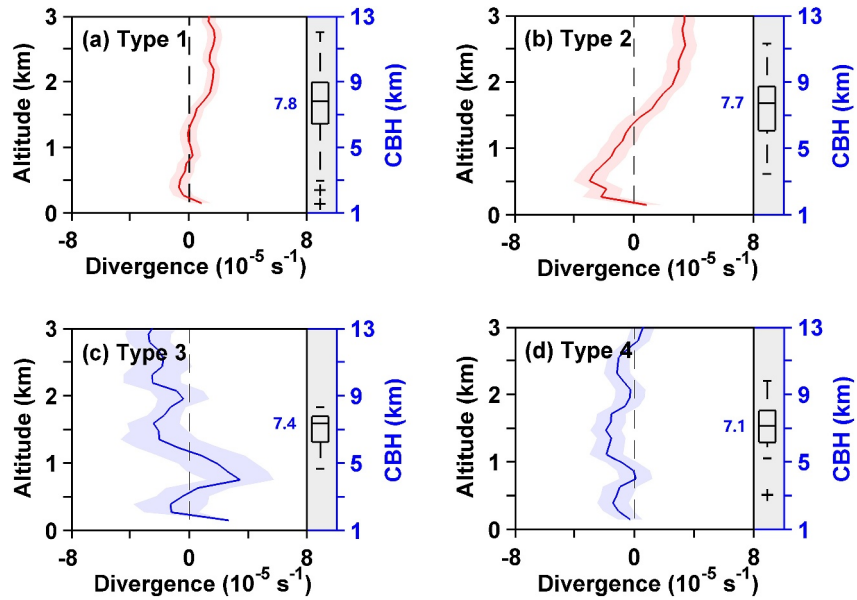

Figure 8. Vertical profiles of 30-min averaged horizontal divergence and cloud-base height (CBH) for the synoptic pattern of panel (a) Type 1, (b) Type 2, (c) Type 3, and (d) Type 4 over the Beijing urban area, which are calculated from the measurements of radar wind profiler Mesonet and cloud radar, respectively. The box-and-whisker plots (gray shading) show the interquartile range (rectangle), extrema (whiskers), outliers (plus sign), the median value (solid line), and the mean value (blue number) of CBH (km).

by the cloud radar matching MCS events. In general, convection in the boundary layer consists of converging thermal plumes near the surface lifted up to the top of the mixed layer, then horizontally diverging under the negative buoyancy of the entrainment layer, forming the boundary layer structure of low-level convergence and high-level divergence. This classical boundary-layer dynamic structure can be observed in severe convective weather (Figures 8a and 8b). Under weak precipitating conditions, the urban roughness (surface friction)-induced convergence constitutes the boundary-layer structure (Figures 8c and 8d). Meanwhile, the lower cloud-base height makes it easier for clouds to couple with the boundary layer.

These results show that the convergence caused by urban roughness promotes the development of MCSs under weak precipitating conditions. However, this effect is not observed under strong precipitating conditions. For a further explanation, in the next section, we quantify the contribution of turbulent friction and surface friction to better understand the dynamic processes.

3.4. Theoretical Analysis of the Urbanization Impact on MCSs

Observational analyses using geostationary satellite data show that the spatial distribution of an MCS and its evolution is highly dependent on the synoptic forcing. To better understand the underlying mechanism of how the urban underlying surface affects the MCS dynamic process, we calculate the contribution of turbulent friction and surface friction under different precipitating conditions using the algorithm described in Section 2.6. Figure 9 shows how friction plays different dominant roles in meteorology. When under strong precipitating condition, the impact of turbulent friction is 0.53 m/s larger than that of weak precipitating condition, and the impact of surface friction is 1.3 m/s smaller than that of weak precipitating condition.

Using high-resolution RWP measurements, we further investigate mean vertical profiles of vertical wind variance, which is often used to indicate the strength of turbulent friction (Figure 10). Figure 10a shows that vertical velocity disturbances due to turbulence restrain urban circulation through rapid mixing in the PBL, inhibiting their impact on UHI-invigorated convective clouds under strong precipitating conditions. The enhanced convergence due to surface friction promotes boundary-layer-cloud coupling, triggering UHI-induced urban circulation under weak precipitating conditions. RWP measurements made in Beijing thus lend credence to the results shown in Figure 9.

21698996, 2024, 24, Downloaded from https://agupubs.onlinelibrary.wiley.com/doi/10.1029/2024JD042294, Wiley Online Library on [01/03/2025]. See the Terms and Conditions (https://onlinelibrary.wiley.com/terms-and-conditions) on Wiley Online Library for rules of use; OA articles are governed by the applicable Creative Commons License

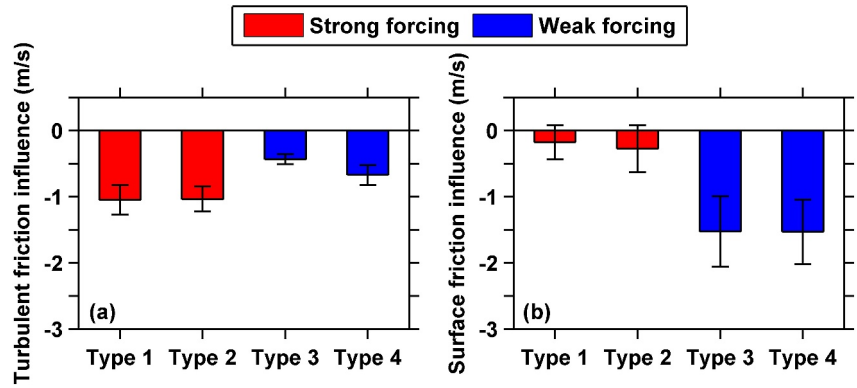

Figure 9. Daytime mean influence of panel (a) turbulent friction in the planetary boundary layer and (b) urban canopy friction on surface wind speed for four different synoptic patterns over the Beijing urban area.

The above analysis suggests that the dynamics play an important role in the evolution of MCS. To quantify the contribution of the dynamic effects to MCS changes, we selected different thermodynamic factors for further analysis (Figure 11). The statistical results indicated that there were significant differences in the contribution of different thermodynamic factors to the evolution of MCS. Under strong precipitating condition, the contribution of turbulence factor and divergence characteristics of 1–3 km are the highest, at 25% and 16.4%, respectively. Under weak precipitating condition, the contribution rates of turbulence factor and sensible heat factor are the highest, at 44.8% and 12%, respectively. This result further confirms the importance of dynamic factors in the evolution of MCS.

3.5. Numerical Experiments of the Urban Impact on MCSs Under Strong and Weak Precipitating Conditions

As mentioned earlier, the dynamic differences in mesoscale synoptic meteorology were captured by observations. Here, two 30-hr simulations (1 September 2020 (Type 4 synoptic pattern) and 11 July 2018 (Type 1 synoptic pattern)) were thus performed to examine the relative role of turbulence under different synoptic forcing conditions (Figure 12). The comparisons of simulated and observed temperature, RH, wind speed, and precipitation in Figures S9–S11 in Supporting Information S1 suggest that simulations are a useful tool in further analyses, although significant deviations still exist between observed and simulated precipitation amounts due to challenges in simulating regional precipitation.

Consistent with the aforementioned observation-based findings, cities have different dynamic structure under different synoptic forcing conditions (Figure 13), that is, under the strong precipitating condition, the divergence characteristic is low-level convergence and high-level divergence, while under weak precipitating condition, fluctuating convergence dominate the dynamic structure of PBL. In addition, as shown in Section 3.4, turbulence also makes a significant contribution to the evolution of MCS. Therefore, the simulation results are used for further analysis from the perspective of turbulence. Figure 14 shows the horizontal structure of turbulence, indicating a difference between the two synoptic forcings. In the mixed layer, convection rolls appear in the strong precipitating case (Figures 14a–14c), and convection cells appear in the weak precipitating case (Figures 14d–14f). In the strong precipitating case, convective rolls in the urban central domain d05 are more linearly arranged than those in the upstream d04 and downstream d06 domains. The dissipation term has a maximum value in the entrainment layer (Figure 15a), which generally corresponds to the height ranges from about 0.8 to 1.1 times \ the PBL height. This suggests that there are more small-scale turbulent vortices in the entrainment layer (Conzemius & Fedorovich, 2006). Moreover, it was found that as turbulence dissipation increases, cloud cover decreases accordingly (Figure S12 in Supporting Information S1). In this case, the larger turbulent dissipation in the city weakens the

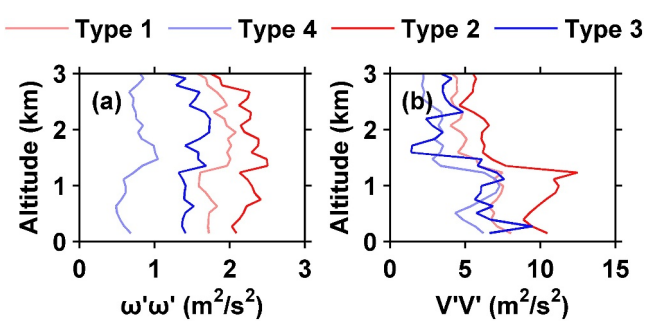

Figure 10. Vertical profiles of panel (a) vertical wind variance and (b) horizontal wind variance under strong (Type 1 and 2) and weak (Type 3 and 4) precipitating conditions, respectively.

21698996, 2024, 24, Downloaded from https://agupubs.onlinelibrary.wiley.com/doi/10.1029/2024JD042294, Wiley Online Library on [01/03/2025]. See the Terms and Conditions (https://onlinelibrary.wiley.com/terms-and-conditions) on Wiley Online Library for rules of use; OA articles are governed by the applicable Creative Commons License

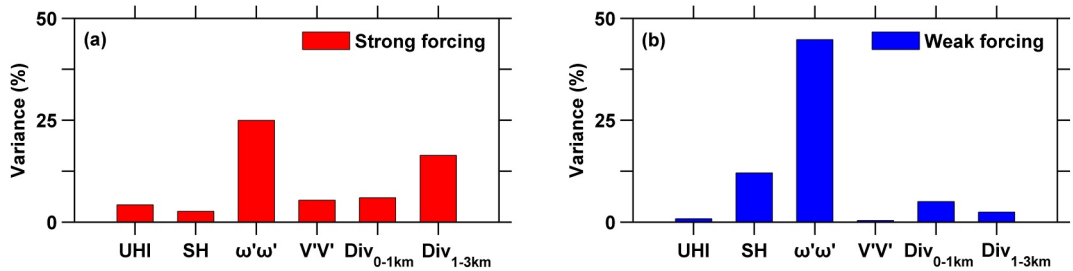

Figure 11. Bar graphs showing the contribution of thermodynamic factors that affect the evolution of mesoscale convective system, including UHI, SH, $\omega'\omega'$, $V'V'$, divergence of 0–1 km (Div_{0-1km}) and 1–3 km (Div_{1-3km}), under (a) strong precipitating condition and (b) weak precipitating condition.

dependence of clouds on the surface and weakens clouds over the city. In the weak precipitating case, convective cells are more obvious downwind of the city. The buoyancy term contributes the most to the turbulent energy of the mixing layer in the weak precipitating case (Figure 15b), with a maximum value near the ground. As it linearly decreases with height, the buoyancy of the entrainment layer becomes negative, indicating that the thermal bubble is the main driving force for the development of the PBL.

To further analyze the impact of urbanization on MCS under different synoptic forcing, the dynamic and heat transfer efficiencies at different altitudes were also calculated and represented by the absolute value of the correlation coefficient |ρ| between u', w', and θ' (Zhao and Zhou, 2021). As shown in Figure 16a, in the strong precipitating condition, there is a higher efficiency of momentum transfer. In this case, the rapid mixing of background winds with the atmosphere in PBL suppresses the development of urban circulation, thereby reducing the impact of urban heat effects. In contrast, under weak precipitating condition, the near surface layer has extremely high heat transfer efficiency (Figure 16b), which promotes the upward transfer of surface heat and thus promotes the development of PBL.

4. Concluding Remarks

The evolution of a MCS has been well recognized to be closely linked to urbanization. Nevertheless, the role of boundary-layer dynamics play in this process remains unclear. The high-density RWP Mesonet in Beijing provides an unprecedented opportunity to fill this knowledge gap from an observational perspective, reinforced with model simulations.

Geostationary satellite data from Fengyun-2 (FY-2) were used to identify and track MCSs occurring over Beijing and its surrounding area. To better isolate the confounding effect of large-scale forcing and urbanization on MCSs, weak and strong precipitating types were distinguished using the T-mode obliquely rotated principal component analysis (T-PCA) algorithm, a widely used objective synoptic classification method. An observational

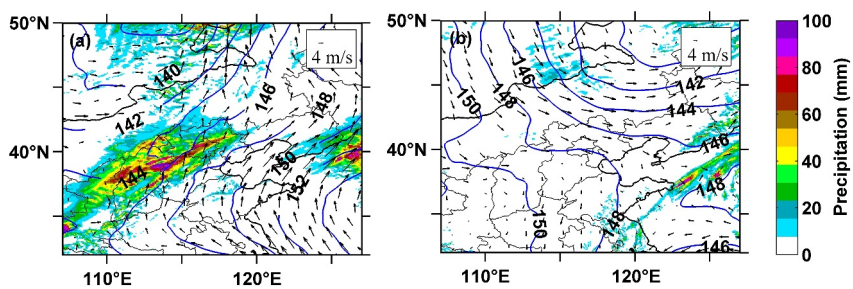

Figure 12. Large-scale distributions of wind (black arrows) and geopotential height (blue contours) at 850-hPa, overlaid with accumulated precipitation amounts (color shading) on panel (a) 11 July 2018 and (b) 1 September 2020.

21698996, 2024, 24, Downloaded from https://agupubs.onlinelibrary.wiley.com/doi/10.1029/2024JD042294, Wiley Online Library on [01/03/2025]. See the Terms and Conditions (https://onlinelibrary.wiley.com/terms-and-conditions) on Wiley Online Library for rules of use; OA articles are governed by the applicable Creative Commons License

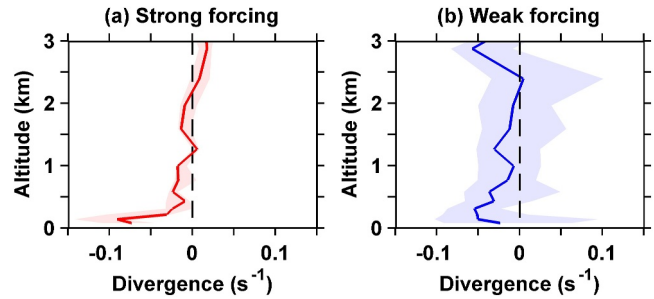

Figure 13. Vertical profiles of averaged horizontal divergence from (a) 0650 BJT to 0720 BJT on 11 July 2018 and from (b) 1,620 to 1650 BJT on 1 September 2020 over the d05 domain, which are calculated from the WRF-LES results.

analysis of the CTT for each MCS event was conducted for each synoptic forcing type using FY-2 data from the warm season (May to September) of 2018 and 2019. Measurements from the RWP Mesonet included 6 stations were used to estimate profiles of divergence over Beijing. Theoretical calculations using wind measurements from the 10-m tower, in combination with sea-level pressure observations, were used to single out the relative contributions of surface friction and turbulent friction.

Under strong precipitating conditions, much lower CTTs were found in the upstream of the Beijing urban area, compared with CTT observations in urban and downstream areas. Coincidently, Mesonet-derived divergence profiles in Beijing had negative values at lower levels of the atmosphere and positive values at higher levels, meaning that large-scale motion played a significant role in the development of MCSs in Beijing. In this case, turbulent friction dominated surface friction in modulating the evolution of MCSs. Given that surface friction is induced by the roughness of the urban canopy, we infer that the impact of urbanization on MCSs is not as large as expected. Under weak precipitating conditions, the CTTs of urban and downstream areas are lower than over upstream areas. Compared with strong precipitating condition, divergence under weak precipitating conditions tends to be dominated by convergence, indicating that convergence caused by surface roughness plays a major role in the enhancement of MCSs in urban and downstream areas. In this case, surface convergence caused by surface friction plays a leading role in regulating the evolution of MCSs.

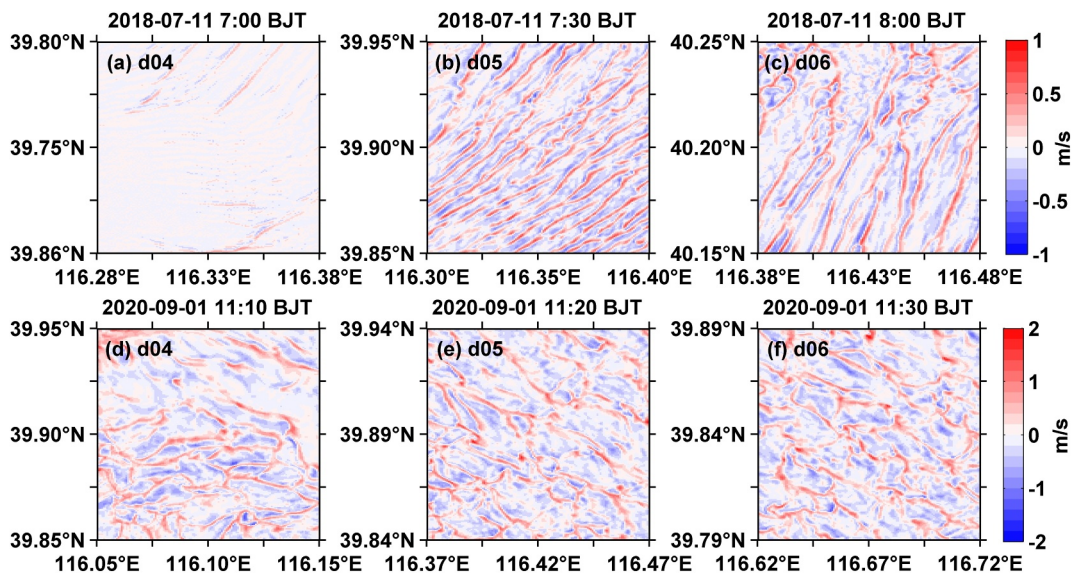

Figure 14. Fields of vertical velocity disturbance at z = 60 m simulated by the WRF-LES for the (a–c) strong precipitating case that occurred from 0700 BJT to 0800 BJT on 11 July 2018 and for the (d–f) weak precipitating case that occurred from 1110 BJT to 1130 BJT on 1 September 2020.

21698996, 2024, 24, Downloaded from https://agupubs.onlinelibrary.wiley.com/doi/10.1029/2024JD042294, Wiley Online Library on [01/03/2025]. See the Terms and Conditions (https://onlinelibrary.wiley.com/terms-and-conditions) on Wiley Online Library for rules of use; OA articles are governed by the applicable Creative Commons License

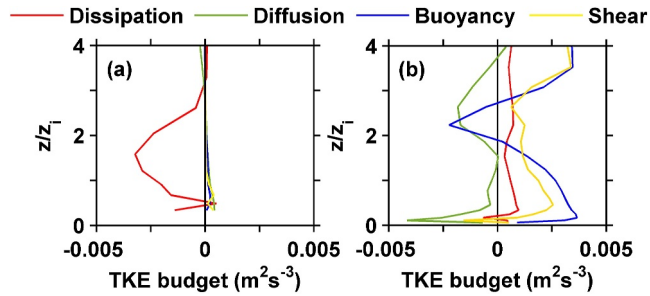

Figure 15. Profiles of averaged magnitudes for the terms of dissipation (red), diffusion (dark green), buoyancy (blue), and shear (yellow) in Equation 8 before cloud occurrence under (a) the strong precipitating case and (b) the weak precipitating case. Note the profiles are averaged over the domain of d05 that are shown in Figure 3, and the height z is normalized by diving the mean planetary boundary layer height (zi).

Furthermore, based on the WRF-LES model, we examined the turbulent structure and the related TKE for two MCS cases: one under strong precipitating conditions and the other under weak precipitating conditions. In the weak precipitating case, buoyancy contributed the most energy to TKE, notably near the urban surface. A buoyancy-induced thermal bubble drove the development of the PBL, reaching a maximum value at 0.3 times the PBL height. Convective cells and MCSs tended to be invigorated over downstream areas, agreeing with satellite observational results. Compared with the weak precipitating case, there was a convection roll turbulent structure over the urban area in the strong precipitating case, where more small-scale turbulent vortices and greater turbulent dissipation were found. This, in turn, led to weak convection, possibly explaining the weakened MCSs in the urban and downstream areas observed by satellite. It can be arguably inferred that turbulence plays different roles in the evolution of MCSs under weak and strong precipitating conditions.

Our findings suggest that convection frequently occurs over urban areas under weak precipitating conditions. It is well recognized that the urban surface is coupled with the PBL and overlying clouds. However, we note that the coupling of the urban PBL and clouds is not well considered in this study. Meanwhile, we also found that the precipitation generated by MCS reaches its maximum downstream in the urban under any synoptic type (Figure S13 in Supporting Information S1), which differs from the distribution characteristics of CTT, that is, under strong (weak) precipitating condition, the average CTT along the urban prevailing wind shows a large upward (downward) trend. This indicates that the mechanism of urban effect on precipitation may differ from that on clouds, for instance, it may also involve microphysical effects of clouds. Therefore, we will use high-resolution temperature and humidity profile observations, as well as cloud microphysical properties, to further investigate this issue in the future.

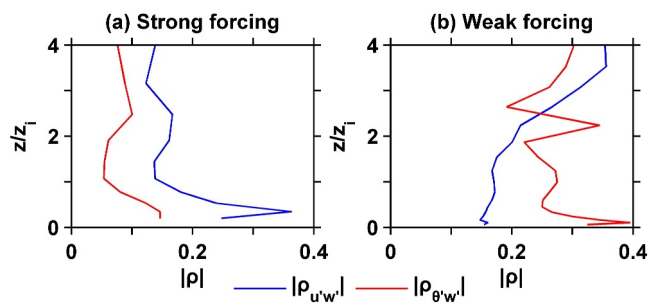

Figure 16. Same as Figure 15, but for the profiles of averaged momentum transfer efficiency (blue line) and heat transfer efficiency (red line) in the domain of d05 for both strong (a) and weak (b) precipitating cases.

21698996, 2024, 24, Downloaded from https://agupubs.onlinelibrary.wiley.com/doi/10.1029/2024JD042294, Wiley Online Library on [01/03/2025]. See the Terms and Conditions (https://onlinelibrary.wiley.com/terms-and-conditions) on Wiley Online Library for rules of use; OA articles are governed by the applicable Creative Commons License

Data Availability Statement

The area-averaged divergence profiles (Guo, Guo and Xian, 2023), synoptic surface meteorological data (CMA, 2023), reanalysis data (ECMWF, 2023), and cloud top temperature data from Fengyun-2 geostationary data (NSMC, 2023) were used in the creation of this manuscript.

Acknowledgments
This research was funded by the National Natural Science Foundation (42030606, 42325501, and 42105090).

References

Agel, L., Barlow, M., Feldstein, S. B., & Gutowski, W. J. (2018). Identification of large-scale meteorological patterns associated with extreme precipitation in the US northeast. *Climate Dynamics*, *50*(5–6), 1819–1839. https://doi.org/10.1007/s00382-017-3724-8

Ai, Y. F., Li, W. B., Meng, Z. Y., & Li, J. (2016). Life cycle characteristics of MCSs in Middle East China tracked by geostationary satellite and precipitation estimates. *Monthly Weather Review*, *144*(7), 2517–2530. https://doi.org/10.1175/MWR-D-15-0197.1

Bellamy, J. C. (1949). Objective calculations of divergence, vertical velocity and vorticity. *Bulletin of the American Meteorological Society*, *30*(2), 45–49. https://doi.org/10.1175/1520-0477-30.2.45

Bornstein, R., & Lin, Q. L. (2000). Urban heat islands and summertime convective thunderstorms in Atlanta: Three case studies. *Atmospheric Environment*, *34*(3), 507–516. https://doi.org/10.1016/S1352-2310(99)00374-X

Bousquet, O., & Chong, M. (2000). The oceanic mesoscale convective system and associated mesovortex observed 12 December 1992 during TOGA-COARE. *Quarterly Journal of the Royal Meteorological Society*, *126*(562), 189–211. https://doi.org/10.1256/smsqj.56209

Chen, D. D., Guo, J. P., Yao, D., Lin, Y. L., Zhao, C. F., Min, M., et al. (2019). Mesoscale convective systems in the Asian monsoon region from advanced Himawari imager: Algorithms and preliminary results. *Journal of Geophysical Research: Atmospheres*, *124*(4), 2210–2234. https://doi.org/10.1029/2018JD029707

Chen, L., & Frauenfeld, O. W. (2016). Impacts of urbanization on future climate in China. *Climate Dynamics*, *47*(1–2), 345–357. https://doi.org/10.1007/s00382-015-2840-6

CMA. (2023). Meteorological data. *China Meteorological Administration*. Retrieved from http://data.cma.cn/

Conzemius, R. J., & Fedorovich, E. (2006). Dynamics of sheared convective boundary layer entrainment. Part I: Methodological background and large-eddy simulations. *Journal of the Atmospheric Sciences*, *63*(4), 1151–1178. https://doi.org/10.1175/jas3691.1

ECMWF. (2023). ERA5-land reanalysis [Dataset]. *European Centre for Medium-Range Weather Forecasts (ECMWF)*. Retrieved from https://cds.climate.copernicus.eu/datasets/reanalysis-era5-pressure-levels?tab=overview

Feng, Z., Leung, L. R., Hagos, S., Houze, R. A., Burleyson, C. D., & Balaguru, K. (2016). More frequent intense and long-lived storms dominate the springtime trend in central US rainfall. *Nature Communications*, *7*(1), 13429. https://doi.org/10.1038/ncomms13429

Feng, Z., Leung, L. R., Liu, N., Wang, J., Houze, R. A., Li, J., et al. (2021). A global high-resolution mesoscale convective system database using satellite-derived cloud tops, surface precipitation, and tracking. *Journal of Geophysical Research: Atmospheres*, *126*(8), e2020JD034202. https://doi.org/10.1029/2020JD034202

Guo, J. P., Guo, X. R., & Xian, T. (2023). Triangle-averaged divergence profiles in Beijing as calculated from three radar wind profilers surrounding Beijing urban area [Dataset]. *Chinese Academy of Meteorological Sciences*. https://doi.org/10.5281/zenodo.7698074

Guo, J. P., Liu, B., Gong, W., Shi, L. J., Zhang, Y., Ma, Y. Y., et al. (2021). Technical note: First comparison of wind observations from ESA's satellite mission Aeolus and ground-based radar wind profiler network of China. *Atmospheric Chemistry and Physics*, *21*(4), 2945–2958. https://doi.org/10.5194/acp-21-2945-2021

Guo, J. P., Miao, Y. C., Zhang, Y., Liu, H., Li, Z. Q., Zhang, W. C., et al. (2016). The climatology of planetary boundary layer height in China derived from radiosonde and reanalysis data. *Atmospheric Chemistry and Physics*, *16*(20), 13309–13319. https://doi.org/10.5194/acp-16-13309-2016

Guo, X., Guo, J., Zhang, D.-L., & Yun, X. (2023b). Vertical divergence profiles as detected by two wind profiler mesonets over East China: Implications for nowcasting convective storms. *Quarterly Journal of the Royal Meteorological Society*, *149*(754), 1629–1649. https://doi.org/10.1002/qj.4474

Han, B. S., Baik, J. J., Park, S. B., & Kwak, K. H. (2019). Large-eddy simulations of reactive pollutant dispersion in the convective boundary layer over flat and urban-like surfaces. *Boundary-Layer Meteorology*, *172*(2), 271–289. https://doi.org/10.1007/s10546-019-00447-2

Hersbach, H., Bell, B., Berrisford, P., Biavati, G., Horányi, A., Muñoz Sabater, J., et al. (2023). ERA5 monthly averaged data on single levels from 1940 to present. *Copernicus Climate Change Service (C3S) Climate Data Store (CDS)*. https://doi.org/10.24381/cds.f17050d7

Hu, X. M., Klein, P. M., Xue, M., Lundquist, J. K., Zhang, F. Q., & Qi, Y. C. (2013). Impact of low-level jets on the nocturnal urban heat island intensity in Oklahoma City. *Journal of Applied Meteorology and Climatology*, *52*(8), 1779–1802. https://doi.org/10.1175/jamc-d-12-0256.1

Huff, F. A., & Changnon, S. A. (1973). Precipitation modification by major urban areas. *Bulletin of the American Meteorological Society*, *54*(12), 1220–1232. https://doi.org/10.1175/1520-0477(1973)054<1220:pmbmua>2.0.co;2

Huth, R., Beck, C., Philipp, A., Demuzere, M., Ustrnul, Z., Cahynova, M., et al. (2008). Classifications of atmospheric circulation patterns. *Annals of the New York Academy of Sciences*, *1146*(1), 105–152. https://doi.org/10.1196/annals.1446.019

Kalnay, E., & Cai, M. (2003). Impact of urbanization and land-use change on climate. *Nature*, *423*(6939), 528–531. https://doi.org/10.1038/nature01675

Kaufmann, R. K., Seto, K. C., Schneider, A., Liu, Z., Zhou, L., & Wang, W. (2007). Climate response to rapid urban growth: Evidence of a human-induced precipitation deficit. *Journal of Climate*, *20*(10), 2299–2306. https://doi.org/10.1175/jcli4109.1

Krueger, O., Feser, F., & Weisse, R. (2019). Northeast Atlantic storm activity and its uncertainty from the late nineteenth to the twenty-first century. *Journal of Climate*, *32*(6), 1919–1931. https://doi.org/10.1175/JCLI-D-18-0505.1

Lee, J. M., Zhang, Y. Y., & Klein, S. A. (2019). The effect of land surface heterogeneity and background wind on shallow cumulus clouds and the transition to deeper convection. *Journal of the Atmospheric Sciences*, *76*(2), 4001–4419. https://doi.org/10.1175/JAS-D-18-0196.1

Lorenz, J. M., Kronenberg, R., Bernhofer, C., & Niyogi, D. (2019). Urban rainfall modification: Observational climatology over Berlin, Germany. *Journal of Geophysical Research: Atmospheres*, *124*(2), 731–746. https://doi.org/10.1029/2018jd028858

Lund, I. A. (1962). Map-pattern classification by statistical methods. *Bulletin of the American Meteorological Society*, *43*(12), 673–&.

Maloney, E. D., & Kiehl, J. T. (2002). Intraseasonal eastern Pacific precipitation and SST variations in a GCM coupled to a slab ocean model. *Journal of Climate*, *15*(21), 2989–3007. https://doi.org/10.1175/1520-0442(2002)015<2989:ieppas>2.0.co;2

Mapes, B. E., & Houze, R. A., Jr. (1993). An integrated view of the 1987 Australin monsoon and its mesoscale convective systems. II: Vertical structure. *Quarterly Journal of the Royal Meteorological Society*, *119*(512), 733–754. https://doi.org/10.1002/qj.49711951207

21698996, 2024, 24, Downloaded from https://agupubs.onlinelibrary.wiley.com/doi/10.1029/2024JD042294, Wiley Online Library on [01/03/2025]. See the Terms and Conditions (https://onlinelibrary.wiley.com/terms-and-conditions) on Wiley Online Library for rules of use; OA articles are governed by the applicable Creative Commons License

Mapes, B. E., & Houze, R. A., Jr. (1995). Diabatic divergence profiles in western Pacific mesoscale convective systems. *Journal of the Atmospheric Sciences*, *52*(10), 1807–1828. https://doi.org/10.1175/1520-0469(1995)052<1807:ddpiwp>2.0.co;2

Miao, S. G., & Chen, F. (2008). Formation of horizontal convective rolls in urban areas. *Atmospheric Research*, *89*(3), 298–304. https://doi.org/10.1016/j.atmosres.2008.02.013

Miao, Y. C., Guo, J. P., Liu, S. H., Liu, H., Li, Z. Q., Zhang, W. C., & Zhai, P. M. (2017). Classification of summertime synoptic patterns in Beijing and their associations with boundary layer structure affecting aerosol pollution. *Atmospheric Chemistry and Physics*, *17*(4), 3097–3110. https://doi.org/10.5194/acp-17-3097-2017

Mills, G. F., Lana, X., & Serra, C. (1994). Catalonian precipitation patterns - Principal component analysis and automated regionalization. *Theoretical and Applied Climatology*, *49*(4), 201–212. https://doi.org/10.1007/bf00867459

Nicholas, R. E., & Battisti, D. S. (2012). Empirical downscaling of high-resolution regional precipitation from large-scale reanalysis fields. *Journal of Applied Meteorology and Climatology*, *51*(1), 100–114. https://doi.org/10.1175/jamc-d-11-04.1

Noh, Y., Cheon, W. G., Hong, S. Y., & Raasch, S. (2003). Improvement of the K-profile model for the planetary boundary layer based on large eddy simulation data. *Boundary-Layer Meteorology*, *107*(2), 401–427. https://doi.org/10.1023/a:1022146015946

NSMC. (2023). Cloud top temperature (CTT) [Dataset]. *National Satellite Meteorological Centre (NSMC)*. Retrieved from http://www.nsmc.org.cn/nsmc/cn/home/index.html

Qian, Y., Chakraborty, T. C., Li, J., Li, D., He, C., Sarangi, C., et al. (2022). Urbanization impact on regional climate and extreme weather: Current understanding, uncertainties, and future research directions. *Advances in Atmospheric Sciences*, *39*(6), 819–860. https://doi.org/10.1007/s00376-021-1371-9

Rai, R. K., Berg, L. K., Kosovic, B., Mirocha, J. D., Pekour, M. S., & Shaw, W. J. (2017). Comparison of measured and numerically simulated turbulence statistics in a convective boundary layer over complex terrain. *Boundary-Layer Meteorology*, *163*(1), 69–89. https://doi.org/10.1007/s10546-016-0217-y

Rana, S., McGregor, J., & Renwick, J. (2019). Dominant modes of winter precipitation variability over Central Southwest Asia and inter-decadal change in the ENSO teleconnection. *Climate Dynamics*, *53*(9–10), 5689–5707. https://doi.org/10.1007/s00382-019-04889-9

Roy, I., & Haigh, J. D. (2011). The influence of solar variability and the quasi-biennial oscillation on lower atmospheric temperatures and sea level pressure. *Atmospheric Chemistry and Physics*, *11*(22), 11679–11687. https://doi.org/10.5194/acp-11-11679-2011

Salesky, S. T., Chamecki, M., & Bou-Zeid, E. (2017). On the nature of the transition between roll and cellular organization in the convective boundary layer. *Boundary-Layer Meteorology*, *163*(1), 41–68. https://doi.org/10.1007/s10546-016-0220-3

Sarangi, C., Tripathi, S. N., Qian, Y., Kumar, S., & Leung, L. R. (2018). Aerosol and urban land use effect on rainfall around cities in Indo-Gangetic Basin from observations and cloud resolving model simulations. *Journal of Geophysical Research: Atmospheres*, *123*(7), 3645–3667. https://doi.org/10.1002/2017jd028004

Serra, C., Mills, G. F., Periago, M. C., & Lana, X. (1996). Winter and Autumn daily precipitation patterns in Catalonia, Spain. *Theoretical and Applied Climatology*, *54*(3–4), 175–186. https://doi.org/10.1007/BF00865160

Shepherd, J. M., Harold, P., & Negri, A. J. (2002). Rainfall modification by major urban areas: Observations from spaceborne rain radar on the TRMM satellite. *Journal of Applied Meteorology*, *41*(7), 689–701. https://doi.org/10.1175/1520-0450(2002)041<0689:RMBMUA>2.0.CO;2

Smagorinsky, J. (1963). General circulation experiments with the primitive equations: I. The basic experiment. *Monthly Weather Review*, *91*(3), 99–164. https://doi.org/10.1175/1520-0493(1963)091<0099:gcewtp>2.3.co;2

Solanki, R., Guo, J., Lv, Y., Zhang, J., Wu, J., Tong, B., & Li, J. (2022). Elucidating the atmospheric boundary layer turbulence by combining UHF Radar wind profiler and radiosonde measurements over urban area of Beijing. *Urban Climate*, *43*, 101151. https://doi.org/10.1016/j.uclim.2022.101151

Stull, R. B. (1988). *An introduction to boundary layer meteorology* (p. 666). Kluwer Academic Publishers.

Taylor, C. M., Belušić, D., Guichard, F., Parker, D. J., Vischel, T., Bock, O., et al. (2017). Frequency of extreme Sahelian storms tripled since 1982 in satellite observations. *Nature*, *544*(7651), 475–478. https://doi.org/10.1038/nature22069

Theeuwes, N. E., Barlow, J. F., Teuling, A. J., Grimmond, C. S. B., & Kotthaus, S. (2019). Persistent cloud cover over mega-cities linked to surface heat release. *Npj Climate and Atmospheric Science*, *2*(1), 15. https://doi.org/10.1038/s41612-019-0072-x

Thielen, J., Wobrock, W., Gadian, A., Mestayer, P. G., & Creutin, J. D. (2000). The possible influence of urban surfaces on rainfall development: A sensitivity study in 2D in the meso-gamma-scale. *Atmospheric Research*, *54*(1), 15–39. https://doi.org/10.1016/S0169-8095(00)00041-7

Uma, K. N., & Rao, T. N. (2009). Diurnal variation in vertical air motion over a tropical station, Gadanki (13.5°N, 79.2°E), and its effect on the estimation of mean vertical air motion. *Journal of Geophysical Research*, *114*(D20), D20106. https://doi.org/10.1029/2009JD012560

Wei, C. C. (2012). RBF neural networks combined with principal component analysis applied to quantitative precipitation forecast for a reservoir watershed during typhoon periods. *Journal of Hydrometeorology*, *13*(2), 722–734. https://doi.org/10.1175/jhm-d-11-03.1

Wu, J., Zha, J., & Zhao, D. (2016). Estimating the impact of the changes in land use and cover on the surface wind speed over the East China Plain during the period 1980–2011. *Climate Dynamics*, *46*(3–4), 847–863. https://doi.org/10.1007/s00382-015-2616-z

Wu, J., Zha, J., Zhao, D., & Yang, Q. (2018). Effects of surface friction and turbulent mixing on long-term changes in the near-surface wind speed over the Eastern China Plain from 1981 to 2010. *Climate Dynamics*, *51*(5–6), 2285–2299. https://doi.org/10.1007/s00382-017-4012-3

Xian, T., Guo, J. P., Zhao, R. Z., Su, T. N., & Li, Z. Q. (2023). The impact of urbanization on mesoscale convective systems in the Yangtze River Delta region of China: Insights gained from observations and modeling. *Journal of Geophysical Research: Atmospheres*, *128*(3), e2022JD037709. https://doi.org/10.1029/2022JD037709

Yan, Y., Miao, Y. C., Guo, J. P., Liu, S. H., Liu, H., Lou, M. Y., et al. (2019). Synoptic patterns and sounding-derived parameters associated with summertime heavy rainfall in Beijing. *International Journal of Climatology*, *39*(3), 1476–1489. https://doi.org/10.1002/joc.5895

Yang, Y., Gao, M., Xie, N. R., & Gao, Z. Q. (2022). Relating anomalous large-scale atmospheric circulation patterns to temperature and precipitation anomalies in the East Asian monsoon region. *Atmospheric Research*, *232*, 104679. https://doi.org/10.1016/j.atmosres.2019.104679

Yu, X. J., Gu, X. H., Kong, D. D., Zhang, Q., Cao, Q., Slater, L. J., et al. (2022). Asymmetrical shift toward less light and more heavy precipitation in an urban agglomeration of east China: Intensification by urbanization. *Geophysical Research Letters*, *49*(2022), 1–12. https://doi.org/10.1029/2021GL097046

Zhang, W., Villarini, G., Vecchi, G. A., & Smith, J. A. (2018). Urbanization exacerbated the rainfall and flooding caused by hurricane Harvey in Houston. *Nature*, *563*(7731), 384–388. https://doi.org/10.1038/s41586-018-0676-z

Zhang, W. C., Guo, J. P., Miao, Y. C., Liu, H., Zhai, P. M., Fang, Z., et al. (2018). On the summertime planetary boundary layer with different thermodynamic stability in China: A radiosonde perspective. *Journal of Climate*, *31*(4), 1451–1465. https://doi.org/10.1175/JCLI-D-17-0231.1

Zhang, Y., Miao, S., Dai, Y., & Bornstein, R. (2017). Numerical simulation of urban land surface effects on summer convective rainfall under different UHI intensity in Beijing. *Journal of Geophysical Research: Atmospheres*, *122*(15), 7851–7868. https://doi.org/10.1002/2017jd026614

21698996, 2024, 24, Downloaded from https://agupubs.onlinelibrary.wiley.com/doi/10.1029/2024JD042294, Wiley Online Library on [01/03/2025]. See the Terms and Conditions (https://onlinelibrary.wiley.com/terms-and-conditions) on Wiley Online Library for rules of use; OA articles are governed by the applicable Creative Commons License

Zhang, Y., Zhou, Q., Lv, S., Jia, S., Tao, F., Chen, D., & Guo, J. (2019). Elucidating cloud vertical structures based on three-year Ka-band cloud radar observations from Beijing, China. *Atmospheric Research*, *222*, 88–99. https://doi.org/10.1016/j.atmosres.2019.02.007

Zhang, Z. T., & Wang, K. C. (2020). Stilling and recovery of the surface wind speed based on observation, reanalysis, and geostrophic wind theory over China from 1960 to 2017. *Journal of Climate*, *33*(10), 3989–4008. https://doi.org/10.1175/jcli-d-19-0281.1

Zhang, Z. T., Wang, K. C., Chen, D. L., Li, J. P., & Dickinson, R. (2019). Increase in surface friction dominates the observed surface wind speed decline during 1973-2014 in the Northern Hemisphere lands. *Journal of Climate*, *32*(21), 7421–7435. https://doi.org/10.1175/jcli-d-18-0691.1

Zhao, Z., & Zhou, B. W. (2021). Non-local mixing of momentum in the daytime convective boundary layer. *Journal of the Meteorological Science*, *41*(05), 631–643.

Zhu, X. L., Ni, G. H., Cong, Z. T., Sun, T., & Li, D. (2016). Impacts of surface heterogeneity on dry planetary boundary layers in an urban-rural setting. *Journal of Geophysical Research: Atmospheres*, *121*(20), 12164–12179. https://doi.org/10.1002/2016JD024982

Zong, L., Yang, Y. J., Gao, M., Wang, H., Wang, P., Zhang, H. L., et al. (2021). Large-scale synoptic drivers of co-occurring summertime ozone and PM2.5 pollution in eastern China. *Atmospheric Chemistry and Physics*, *21*(11), 9105–9124. https://doi.org/10.5194/acp-21-9105-2021

Zveryaev, I. I. (2006). Seasonally varying modes in long-term variability of European precipitation during the 20th century. *Journal of Geophysical Research*, *111*, D21. https://doi.org/10.1029/2005jd006821

21698996, 2024, 24, Downloaded from https://agupubs.onlinelibrary.wiley.com/doi/10.1029/2024JD042294, Wiley Online Library on [01/03/2025]. See the Terms and Conditions (https://onlinelibrary.wiley.com/terms-and-conditions) on Wiley Online Library for rules of use; OA articles are governed by the applicable Creative Commons License